Journal of Fundamental and Applied Research **Vol. 5**, Issue 4 (2025) **20250030**

Received: 03 November 2025 / Accepted: 17 December 2025
Published online: 22 December 2025
© 2025 The Author(s)

Optical depth dependence of X-ray spectral hardening in compact coronae: A general relativistic Monte Carlo study

Akhror Ortiqov[1, *]

[1] *School of Humanities, Natural and Social Sciences, New Uzbekistan University, Tashkent 100001, Uzbekistan*

Abstract. We present a systematic study of X-ray spectral formation in compact spherical coronae surrounding stellar-mass black holes using general relativistic Monte Carlo simulations. We investigate the optical depth dependence of Comptonization for black hole spins ranging from non-rotating ($a = 0.0$) to near-extremal ($a = 0.998$) and optical depths $\tau = 0.2$–2.0 in a compact corona with radius $R = 6\,GM/c^2$. Our simulations employ full Kerr geodesic calculations coupled with Klein-Nishina scattering and track both spectral evolution and the separation between thermal and Comptonized components. We find that the photon index decreases systematically from $\Gamma \approx 3.6$–3.7 at $\tau = 0.2$ to $\Gamma \approx 1.6$–1.7 at $\tau = 2.0$, approximately following $\Gamma \propto \tau^{-0.45}$, consistent with classical Comptonization theory but modified by general relativistic effects. At low optical depths, we observe significant spin-dependent spectral hardening, with the near-extremal case ($a = 0.998$) showing $\Gamma \approx 2.6$ compared to $\Gamma \approx 3.6$ for the non-rotating case at $\tau = 0.2$, a difference $\Delta\Gamma \approx 1.0$ attributed to enhanced photon capture from the inner disc via strong gravitational light bending. The energy-dependent Comptonization fraction transitions from thermal-dominated emission at soft energies to Comptonization-dominated emission above $\sim$5–10 keV. These results provide theoretical predictions for interpreting X-ray binary spectra and demonstrate the importance of including general relativistic effects in compact corona models.

Key words: accretion, accretion discs, black hole physics, radiative transfer, X-rays: binaries, relativistic processes, numerical methods.

I. INTRODUCTION

The hard X-ray emission from accreting black hole systems, both stellar-mass X-ray binaries (XRBs) and active galactic nuclei (AGN), is understood to arise from Compton up-scattering of soft thermal photons from the accretion disc by hot electrons in a corona surrounding the disc. This Comptonization process produces the characteristic power-law spectra observed in the 2–10 keV band, with photon indices typically ranging from $\Gamma \approx 1.5$–2.5 in XRBs. The spectral shape is primarily determined by the electron temperature $T_{\rm e}$ and optical depth τ of the corona, as described by classical Comptonization theory developed by Sunyaev & Titarchuk [1] and subsequent works. However, in the strong gravitational field near black holes, general relativistic (GR) effects can significantly modify photon trajectories and energy transport, particularly for compact coronae located close to the horizon.

Observationally, XRB spectra in the hard state show power-law emission extending from soft X-rays to hundreds of keV, with exponential cutoffs typically around 100–300 keV indicating coronal temperatures of $T_{\rm e} \approx 50$–$150\,{\rm keV}$. The geometry and location of the corona remain uncertain, with proposed configurations including sandwich-layer geometries, lamppost coronae at heights of 5–10 gravitational radii, and compact spherical or conical coronae near the inner disc truncation radius [2, 3]. Recent X-ray reverberation studies and spectral state transition observations provide evidence for compact coronae located within a few gravitational radii of the black hole, with the corona contracting during state transitions [4, 5]. Spectral fitting with models such as NTHCOMP [6] or COMPTT [7] can constrain the temperature and optical depth, but these analytical models typically neglect GR effects or treat them only approximately.

Recent polarization measurements from the Imaging X-ray Polarimetry Explorer (IXPE) have provided new constraints on coronal geometry by detecting significant polarization in the 2–8 keV band [8–10]. The unexpectedly high polarization degree

* Corresponding author: a.ortiqov@newuu.uz

($\sim$4% in the hard state) measured in Cygnus X-1 suggests that the corona is extended in the same direction as the accretion disc rather than configured as a compact lamppost, constraining viable coronal geometries [8]. These observations suggest that scattering in optically thin to moderately thick coronae plays a crucial role in shaping both the spectral and polarimetric properties. Theoretical modeling of these systems therefore requires coupling of GR ray-tracing with accurate Compton scattering physics, including Klein-Nishina cross-sections and polarization transport.

Several Monte Carlo codes have been developed to address this problem. MONK (Monte Carlo code for disc-corona systems in Kerr geometry) performs full GR ray-tracing combined with Klein-Nishina scattering and has been successfully applied to model AGN and XRB systems [11], with recent extensions to study coronal geometry in different spectral states [12]. Other codes such as the models by Schnittman & Krolik [13, 14] and the STOKES code [15, 16] employ similar approaches for polarization modeling. However, systematic parameter space studies exploring the interplay between optical depth and black hole spin in compact geometries remain limited.

In this paper, we present results from a systematic exploration of optical depth effects on X-ray spectral formation in compact spherical coronae. We focus on stellar-mass black holes with three representative spin values: $a = 0.0$ (Schwarzschild), $a = 0.7$ (moderate rotation), and $a = 0.998$ (near-extremal Kerr). For each spin, we vary the optical depth from $\tau = 0.2$ to $\tau = 2.0$, spanning the range from optically thin to moderately thick coronae typical of XRB hard states. Our compact corona geometry with radius $R = 6\,GM/c^2$ is motivated by recent observational constraints suggesting that coronae in XRBs are located close to the inner disc.

The paper is organized as follows. Section II describes our numerical methods and simulation setup. Section III presents the main results, including spectral evolution with optical depth, photon index measurements, and component separation. Section IV discusses the physical interpretation and comparison with classical Comptonization theory. Section V summarizes our conclusions and outlines future work.

II. METHODS

A. Monte Carlo Radiation Transfer Code

We employ the MONK code [11], which performs Monte Carlo radiation transfer simulations in Kerr spacetime. The code operates in three stages, described below.

1. Stage 1: Geodesic Pre-computation

Photon geodesics from the accretion disc to the corona and infinity are pre-computed by solving the geodesic equations in Boyer-Lindquist coordinates (t, r, θ, ϕ). In the Kerr metric with signature $(-,+,+,+)$, the line element is:

$$\begin{aligned} ds^2 = &-\left(1 - \frac{2Mr}{\Sigma}\right) dt^2 - \frac{4Mra\sin^2\theta}{\Sigma} dt d\phi \\ &+ \frac{\Sigma}{\Delta} dr^2 + \Sigma d\theta^2 + \frac{A\sin^2\theta}{\Sigma} d\phi^2, \end{aligned} \tag{1}$$

where M is the black hole mass, a is the dimensionless spin parameter, and

$$\Sigma = r^2 + a^2\cos^2\theta, \tag{2}$$

$$\Delta = r^2 - 2Mr + a^2, \tag{3}$$

$$A = (r^2 + a^2)^2 - a^2\Delta\sin^2\theta. \tag{4}$$

Photon trajectories are characterized by three conserved quantities: the specific energy $\mathcal{E} = -p_t$, the axial component of angular momentum $\mathcal{L} = p_\phi$, and the Carter constant $\mathcal{Q}$, where p_μ is the four-momentum. These lead to the first-order geodesic equations:

$$\Sigma\frac{dr}{d\lambda} = \pm\sqrt{R(r)}, \tag{5}$$

$$\Sigma\frac{d\theta}{d\lambda} = \pm\sqrt{\Theta(\theta)}, \tag{6}$$

$$\Sigma\frac{d\phi}{d\lambda} = -\left(a\mathcal{E} - \frac{\mathcal{L}}{\sin^2\theta}\right) + \frac{a}{\Delta}P(r), \tag{7}$$

$$\Sigma\frac{dt}{d\lambda} = -a\left(a\mathcal{E}\sin^2\theta - \mathcal{L}\right) + \frac{r^2 + a^2}{\Delta}P(r), \tag{8}$$

 Copyright © 2025

where λ is the affine parameter, and

$$R(r) = P(r)^2 - \Delta\left[\mathcal{Q} + (\mathcal{L} - a\mathcal{E})^2\right], \tag{9}$$

$$\Theta(\theta) = \mathcal{Q} - \cos^2\theta\left[a^2\mathcal{E}^2 + \frac{\mathcal{L}^2}{\sin^2\theta}\right], \tag{10}$$

$$P(r) = \mathcal{E}(r^2 + a^2) - a\mathcal{L}. \tag{11}$$

The geodesic grid is stored with typical resolution of $n_r = 200$ radial bins, $n_\theta = 50$ polar angle bins, and $n_\phi = 50$ azimuthal bins, covering the disc region from the innermost stable circular orbit (ISCO) to the outer radius $r_{\rm out} = 100\,GM/c^2$.

2. Stage 2: Monte Carlo Photon Propagation

Thermal photons are sampled from the disc surface according to the Novikov-Thorne flux distribution [17, 18]. The disc effective temperature as a function of radius is given by:

$$T_{\rm eff}(r) = \left[\frac{3GM\dot{M}}{8\pi\sigma r^3} f(r)\right]^{1/4}, \tag{12}$$

where σ is the Stefan-Boltzmann constant, and $f(r)$ is the relativistic correction factor:

$$f(r) = 1 - \sqrt{\frac{r_{\rm ISCO}}{r}}, \tag{13}$$

valid for $r > r_{\rm ISCO}$. The flux emitted from an annulus at radius r is:

$$F_{\rm disc}(r) = \sigma T_{\rm eff}^4(r) = \frac{3GM\dot{M}}{8\pi r^3} f(r). \tag{14}$$

We apply a color correction factor $f_{\rm col} = 1.7$ to account for atmospheric hardening, such that the observed color temperature is $T_{\rm col} = f_{\rm col} T_{\rm eff}$.

Photons that enter the corona undergo Compton scattering with thermal electrons distributed according to the Maxwell-Jüttner distribution at temperature $T_{\rm e}$:

$$n_{\rm e}(p) = \frac{p^2 \exp(-\gamma/\theta)}{4\pi m_{\rm e}^3 c^3 \theta K_2(1/\theta)}, \tag{15}$$

where $p = |\boldsymbol{p}|$ is the electron momentum magnitude, $\gamma = \sqrt{1 + p^2/(m_{\rm e}c)^2}$ is the Lorentz factor, $\theta = kT_{\rm e}/(m_{\rm e}c^2)$ is the dimensionless temperature, and K_2 is the modified Bessel function of the second kind.

The Klein-Nishina differential cross-section for Compton scattering in the electron rest frame is:

$$\frac{d\sigma_{\rm KN}}{d\Omega} = \frac{r_0^2}{2}\left(\frac{x'}{x}\right)^2\left(\frac{x}{x'} + \frac{x'}{x} - \sin^2\theta_s\right), \tag{16}$$

where $r_0 = e^2/(m_{\rm e}c^2)$ is the classical electron radius, $x = E/(m_{\rm e}c^2)$ and $x' = E'/(m_{\rm e}c^2)$ are the dimensionless photon energies before and after scattering, θ_s is the scattering angle, and the energy change is given by:

$$x' = \frac{x}{1 + x(1 - \cos\theta_s)}. \tag{17}$$

The total Klein-Nishina cross-section is:

$$\sigma_{\rm KN}(x) = \frac{3\sigma_{\rm T}}{4}\left[\frac{1+x}{x^3}\left(\frac{2x(1+x)}{1+2x} - \ln(1+2x)\right) + \frac{\ln(1+2x)}{2x} - \frac{1+3x}{(1+2x)^2}\right], \tag{18}$$

where $\sigma_{\rm T} = 8\pi r_0^2/3 = 6.65 \times 10^{-25}\,{\rm cm}^2$ is the Thomson cross-section.

Photon polarization is tracked using the Walker-Penrose formalism [19, 20] adapted to Kerr geometry. The scattering process continues until photons either escape to infinity, return to the disc, or fall into the black hole. The coronal optical depth is defined as:

$$\tau = n_{\rm e}\sigma_{\rm T} L_{\rm cor}, \tag{19}$$

where $n_{\rm e}$ is the electron number density and $L_{\rm cor} = 2R$ is the characteristic corona size (diameter of the spherical corona).

Copyright © 2025

3. Stage 3: Spectral Extraction

Escaping photons are binned by energy and inclination angle to produce observer-frame spectra. The flux is calculated in $N_{\rm bin} = 50$ logarithmic energy bins from $E_{\rm min} = 0.1\,\mathrm{keV}$ to $E_{\rm max} = 100\,\mathrm{keV}$. Photons are also tagged by the number of scatterings $n_{\rm sca}$ they underwent, allowing separation of the thermal component ($n_{\rm sca} = 0$, unscattered photons) from the Comptonized component ($n_{\rm sca} \geq 1$, scattered photons).

B. Physical Parameters

We consider a stellar-mass black hole with mass $M = 10\,\mathrm{M}_\odot$ and accretion rate $\dot{M} = 0.1\,\dot{M}_{\rm Edd}$, where the Eddington accretion rate is:

$$\dot{M}_{\rm Edd} = \frac{L_{\rm Edd}}{\eta c^2} = \frac{4\pi GM}{\eta \kappa_{\rm es} c}, \tag{20}$$

with radiative efficiency $\eta = 0.1$ and electron scattering opacity $\kappa_{\rm es} = 0.34\,\mathrm{cm^2\,g^{-1}}$.

The accretion disc follows the Novikov-Thorne model with inner radius at the ISCO and outer radius at $r_{\rm out} = 100\,GM/c^2$. For a Kerr black hole, the ISCO radius is given by:

$$r_{\rm ISCO} = 3 + Z_2 \mp \sqrt{(3 - Z_1)(3 + Z_1 + 2Z_2)}, \tag{21}$$

where the minus sign applies for prograde orbits ($a > 0$), and

$$Z_1 = 1 + (1 - a^2)^{1/3}[(1 + a)^{1/3} + (1 - a)^{1/3}], \tag{22}$$

$$Z_2 = \sqrt{3a^2 + Z_1^2}. \tag{23}$$

For our three spin values:

- $a = 0.0$ (Schwarzschild): $r_{\rm ISCO} = 6.0\,GM/c^2$
- $a = 0.7$ (moderate): $r_{\rm ISCO} \approx 3.4\,GM/c^2$
- $a = 0.998$ (near-extremal): $r_{\rm ISCO} \approx 1.2\,GM/c^2$

The corona is modeled as a spherical region with outer radius $R = 6\,GM/c^2$, centered on the black hole and extending from the event horizon to this radius. The corona contains thermal electrons in a zero-angular-momentum observer (ZAMO) frame with temperature $T_{\rm e} = 100\,\mathrm{keV}$, representative of typical XRB coronal temperatures. The optical depth τ is varied across four values: $\tau = 0.2, 0.5, 1.0, 2.0$.

Each simulation samples photons from the entire disc-corona system with $n_{\rm ph} = 2000$ photons per geodesic grid point, resulting in $\sim 10^7$ photons tracked to infinity. Spectra are integrated over all viewing angles and binned in energy to produce total flux distributions.

C. Spectral Analysis

From the simulated spectra, we extract the photon index Γ by fitting a power-law model:

$$F(E) = NE^{-\Gamma}, \tag{24}$$

in the 2–10 keV energy band. This band is chosen to avoid the soft excess below 2 keV and the high-energy rollover above 10 keV, focusing on the power-law-dominated region typically used in observational studies.

Fits are performed in logarithmic space using linear regression:

$$\log F(E) = \log N - \Gamma \log E, \tag{25}$$

such that Γ is the negative slope of the best-fit line. The reduced chi-squared statistic is calculated as:

$$\chi^2_{\rm red} = \frac{1}{N_{\rm dof}} \sum_{i=1}^{N_{\rm bin}} \frac{(F_i - F_{\rm model,i})^2}{F_{\rm model,i}}, \tag{26}$$

Copyright © 2025

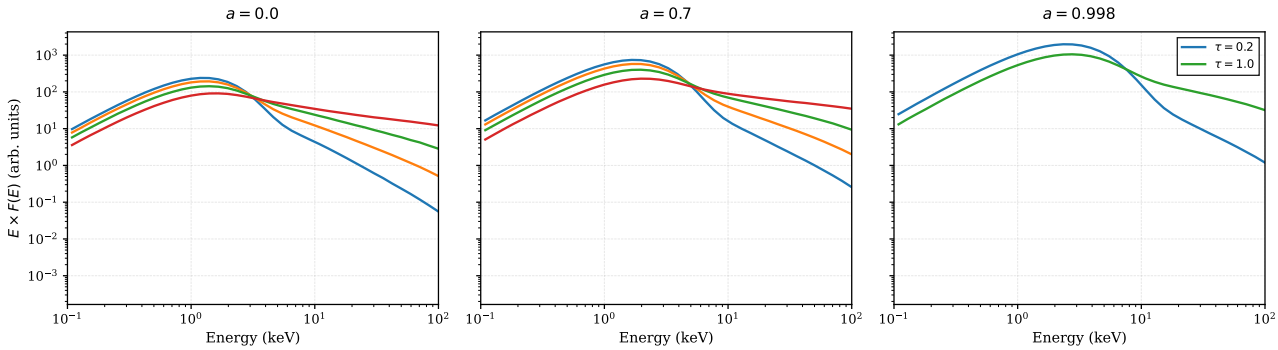


FIG. 1: Spectral evolution with optical depth for three black hole spins. Each panel shows $E \times F(E)$ versus energy for four optical depths ($\tau = 0.2, 0.5, 1.0, 2.0$) at fixed spin. *Left:* $a = 0.0$ (Schwarzschild). *Middle:* $a = 0.7$ (moderate spin). *Right:* $a = 0.998$ (near-extremal). Systematic spectral hardening with increasing τ is evident in all cases, with the near-extremal spin showing the hardest spectra at low optical depths due to enhanced photon capture from the inner disc.

where $N_{\rm dof} = N_{\rm bin} - 2$ is the number of degrees of freedom (number of bins minus two fit parameters).

We also separately analyze the thermal and Comptonized components. The Comptonization fraction as a function of energy is defined as:

$$f_{\rm comp}(E) = \frac{F_{\rm comp}(E)}{F_{\rm thermal}(E) + F_{\rm comp}(E)}, \tag{27}$$

where $F_{\rm thermal}(E)$ is the flux from photons with $n_{\rm sca} = 0$ and $F_{\rm comp}(E)$ is the flux from photons with $n_{\rm sca} \geq 1$.

III. RESULTS

A. Spectral Evolution with Optical Depth

Figure 1 presents the spectral evolution with optical depth for the three spin values studied. Each panel shows the energy-flux product $E \times F(E)$ versus energy for four optical depths at fixed spin. This representation emphasizes the peak of the spectral energy distribution and facilitates comparison across different optical depths.

For the Schwarzschild case ($a = 0.0$, left panel), we observe systematic spectral hardening as optical depth increases. At $\tau = 0.2$, the spectrum peaks around 1–2 keV, characteristic of a disc-dominated soft state. As τ increases to 0.5, the spectral peak shifts to higher energies and the spectrum flattens in the 2–10 keV band, indicating enhanced Comptonization. By $\tau = 1.0$, the power-law component dominates across the full energy range, and at $\tau = 2.0$, the spectrum becomes quite hard with significant flux extending above 50 keV.

The moderate spin case ($a = 0.7$, middle panel) shows similar trends but with overall higher normalization due to increased photon capture by the corona. The enhanced light bending in the Kerr metric funnels more photons from the inner disc into the compact corona compared to the Schwarzschild case. The spectral shapes are qualitatively similar to the $a = 0.0$ case, but the transition from thermal to Comptonization dominance occurs at slightly different optical depths.

The near-extremal spin case ($a = 0.998$, right panel) exhibits the most dramatic differences. Even at $\tau = 0.2$, the spectrum is significantly harder than the corresponding cases at lower spins. The very small ISCO radius ($1.2\,GM/c^2$) places the hottest disc regions well inside the compact corona, and the extreme light bending captures a large fraction of these inner-disc photons. At $\tau = 1.0$, the spectrum is already quite hard, approaching the shape seen at $\tau = 2.0$ for lower spins.

B. Photon Index versus Optical Depth

Figure 2 quantifies the spectral hardening by showing the photon index Γ as a function of optical depth. The left panel displays the photon index measured from the total spectrum (thermal plus Comptonized), while the right panel shows the photon index from the Comptonized component alone.

For the total spectrum, we find a clear monotonic decrease in Γ with increasing τ for all spin values. The Schwarzschild case yields $\Gamma = 3.59 \pm 0.11$ at $\tau = 0.2$, decreasing to $\Gamma = 2.69 \pm 0.07$ at $\tau = 0.5$, $\Gamma = 2.07 \pm 0.04$ at $\tau = 1.0$, and $\Gamma = 1.60 \pm 0.01$ at

Copyright © 2025

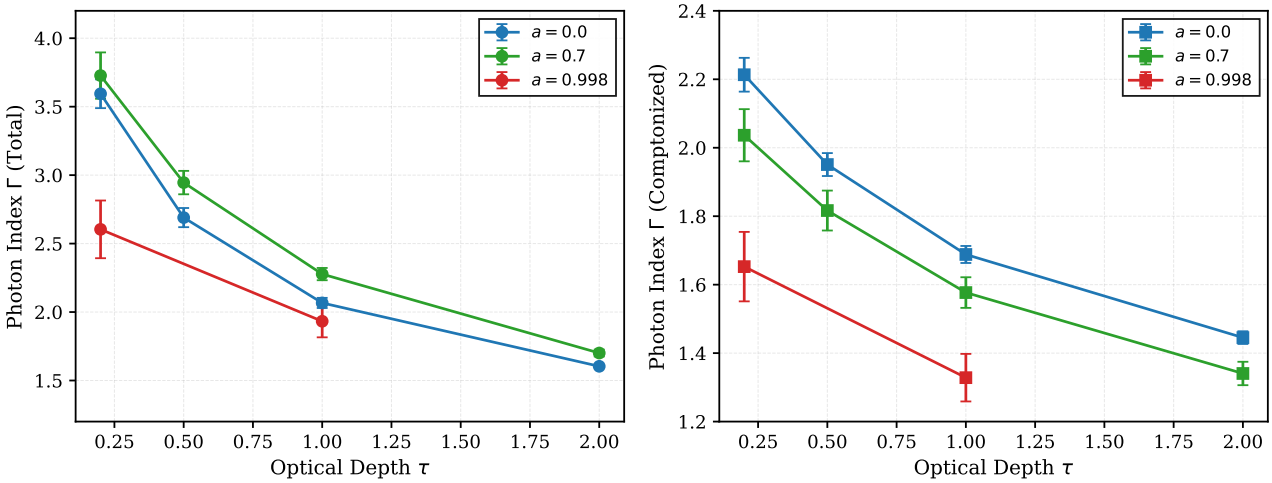


FIG. 2: Photon index versus optical depth for all three spins. *Left panel:* Total spectrum (thermal plus Comptonized). *Right panel:* Comptonized component only. Error bars represent fit uncertainties from power-law fitting in the 2–10 keV band using Eq. (25). The systematic decrease of Γ with increasing τ is consistent with classical Comptonization theory. Spin-dependent effects are most pronounced at low τ, where the near-extremal case shows $\Gamma \approx 2.6$ compared to $\Gamma \approx 3.6$ for the Schwarzschild case, a difference $\Delta\Gamma \approx 1.0$ attributable to general relativistic light bending.

$\tau = 2.0$. This span of $\Delta\Gamma \approx 2.0$ over one decade in optical depth is consistent with classical Comptonization theory predictions (see Sec. IV A).

The moderate spin case ($a = 0.7$) follows a similar trend with slightly higher Γ values at low optical depths: from $\Gamma = 3.73 \pm 0.17$ at $\tau = 0.2$ to $\Gamma = 1.70 \pm 0.03$ at $\tau = 2.0$. The near-extremal case ($a = 0.998$) shows significantly lower Γ values at the same optical depths: $\Gamma = 2.60 \pm 0.21$ at $\tau = 0.2$ and $\Gamma = 1.93 \pm 0.12$ at $\tau = 1.0$. This spin-dependent behavior is most pronounced at low optical depths and becomes less significant at high τ.

The dependence can be approximated by a power-law relation:

$$\Gamma(\tau) = \Gamma_0 \tau^{-\alpha}, \tag{28}$$

where fitting our $a = 0.7$ data yields $\Gamma_0 \approx 2.8$ and $\alpha \approx 0.45$ in the range $\tau = 0.2$–2.0.

The Comptonized component alone (right panel) shows systematically harder spectra across all cases. At low τ, the Comptonized photons have $\Gamma_{\rm comp} \approx 2.0$–$2.2$, while the total spectrum has $\Gamma \approx 3.5$–3.7 due to the dominant contribution of unscattered thermal photons. At high τ, the total and Comptonized indices converge as nearly all photons undergo scattering. This convergence is evident in the $\tau = 2.0$ case where $\Gamma \approx \Gamma_{\rm comp} \approx 1.4$–$1.7$ depending on spin.

The error bars on the photon index measurements scale inversely with optical depth, as higher τ produces more scattered photons and better statistics in the Comptonized component. The larger uncertainties at $a = 0.998$ reflect the greater complexity of photon paths in the extreme Kerr geometry.

C. Component Evolution

Figure 3 illustrates the evolution of thermal versus Comptonized components for the fiducial $a = 0.7$ case. The left panel overlays the thermal (dashed lines) and Comptonized (solid lines) components for each optical depth. At $\tau = 0.2$, the thermal component dominates below $\sim$5 keV, while the Comptonized component dominates above this energy. As τ increases, the Comptonized component strengthens and extends to lower energies, eventually dominating across the entire band at $\tau = 2.0$.

The right panel quantifies this transition through the energy-dependent Comptonization fraction $f_{\rm comp}(E)$ [Eq. (27)]. At low energies (0.1–1 keV), $f_{\rm comp}$ ranges from $\sim$0.1 at $\tau = 0.2$ to $\sim$0.6 at $\tau = 2.0$, indicating that thermal emission remains significant even at moderate optical depths. At intermediate energies (2–10 keV), $f_{\rm comp}$ increases strongly with both energy and optical depth. Above 20 keV, $f_{\rm comp}$ approaches unity for all cases, as thermal disc emission becomes negligible at these high energies and Comptonization dominates completely.

The energy dependence of $f_{\rm comp}$ reflects the combined effects of the seed photon energy distribution and the energy-dependent scattering cross-section [Eq. (18)]. Lower-energy seed photons from the outer disc regions are less likely to be Comptonized at low τ, while higher-energy photons preferentially arise from Compton scattering in the corona.

Copyright © 2025

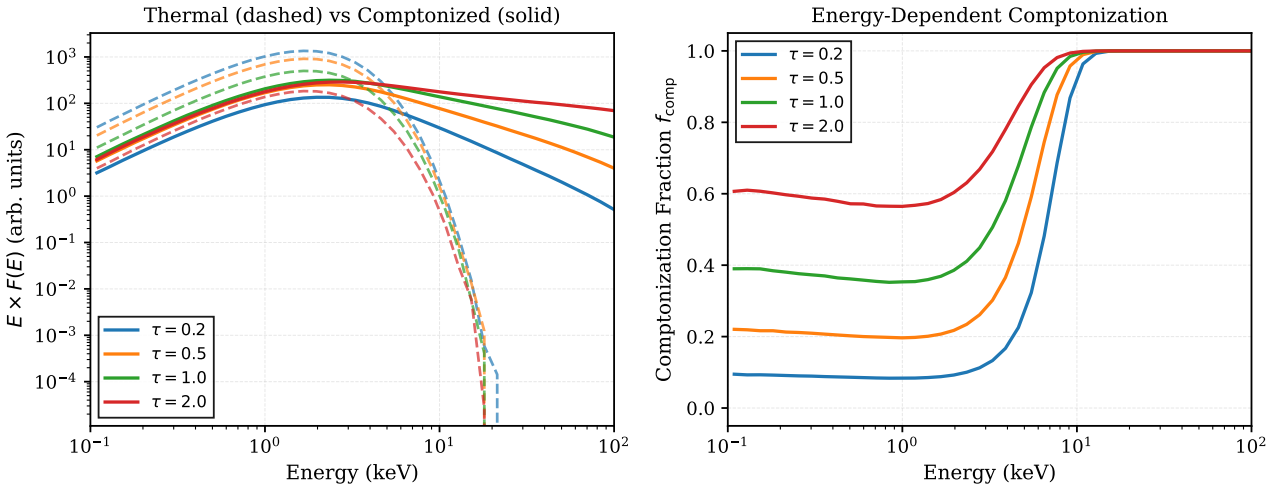


FIG. 3: Component evolution for $a = 0.7$. *Left panel:* Thermal (dashed) versus Comptonized (solid) components for each optical depth. The thermal component consists of photons with $n_{\rm sca} = 0$, while the Comptonized component includes all scattered photons ($n_{\rm sca} \geq 1$). *Right panel:* Energy-dependent Comptonization fraction $f_{\rm comp}(E)$ defined in Eq. (27). The transition from thermal-dominated to Comptonization-dominated emission occurs at higher energies and lower optical depths, reflecting the seed photon energy distribution and the energy-dependent Klein-Nishina cross-section [Eq. (18)].

D. Spin-Dependent Effects

Figure 4 compares spectral shapes at fixed optical depth but varying spin. At $\tau = 0.2$ (top-left panel), the spin dependence is most dramatic. The Schwarzschild and moderate-spin cases produce soft, disc-dominated spectra peaking around 1–2 keV, while the near-extremal case shows significant hardening with enhanced high-energy flux. This difference arises from two GR effects: (i) the smaller ISCO radius at high spin [Eq. (21)] provides hotter seed photons from the inner disc [Eq. (12)], and (ii) the stronger gravitational light bending increases the fraction of these photons captured by the corona.

At $\tau = 0.5$ (top-right panel), the spin effects remain visible but are somewhat reduced as Comptonization begins to dominate all cases. By $\tau = 1.0$ (bottom-left panel), the spectra become more similar in shape, though normalization differences persist due to varying photon capture efficiencies. At $\tau = 2.0$ (bottom-right panel), all three spins produce hard, Comptonization-dominated spectra with similar power-law slopes, and the spin dependence is minimal.

These results suggest that GR effects on spectral shape are most important when thermal emission contributes significantly to the total spectrum. In this regime, the different inner disc temperatures and photon capture geometries across spins lead to measurable spectral differences. At high optical depths where multiple scattering erases the memory of seed photon properties, the spectra converge toward a universal Comptonization shape determined primarily by τ and $T_{\rm e}$.

IV. DISCUSSION

A. Comparison with Classical Comptonization Theory

The Sunyaev-Titarchuk formalism [1, 7] predicts that the photon index in unsaturated Comptonization depends on the Comptonization parameter:

$$y \approx \tau \max\left[4\theta, 16\theta^2\right], \tag{29}$$

where $\theta = kT_{\rm e}/(m_{\rm e}c^2)$ is the dimensionless electron temperature. For our fiducial temperature $T_{\rm e} = 100\,\mathrm{keV}$, we have $\theta = 100/511 = 0.196$, placing us in the regime where $y \approx 4\tau\theta \approx 0.78\tau$. Recent refinements to Comptonization theory for mildly relativistic electrons [21, 22] provide empirical relations that improve agreement with numerical simulations, though the basic τ–θ dependence remains robust.

The photon index in the unsaturated regime ($y \lesssim 1$) can be approximated as:

$$\Gamma \approx \frac{9}{4}\left(\frac{1}{y} + 1\right)^{-1/2} + \frac{1}{2}, \tag{30}$$

Copyright © 2025

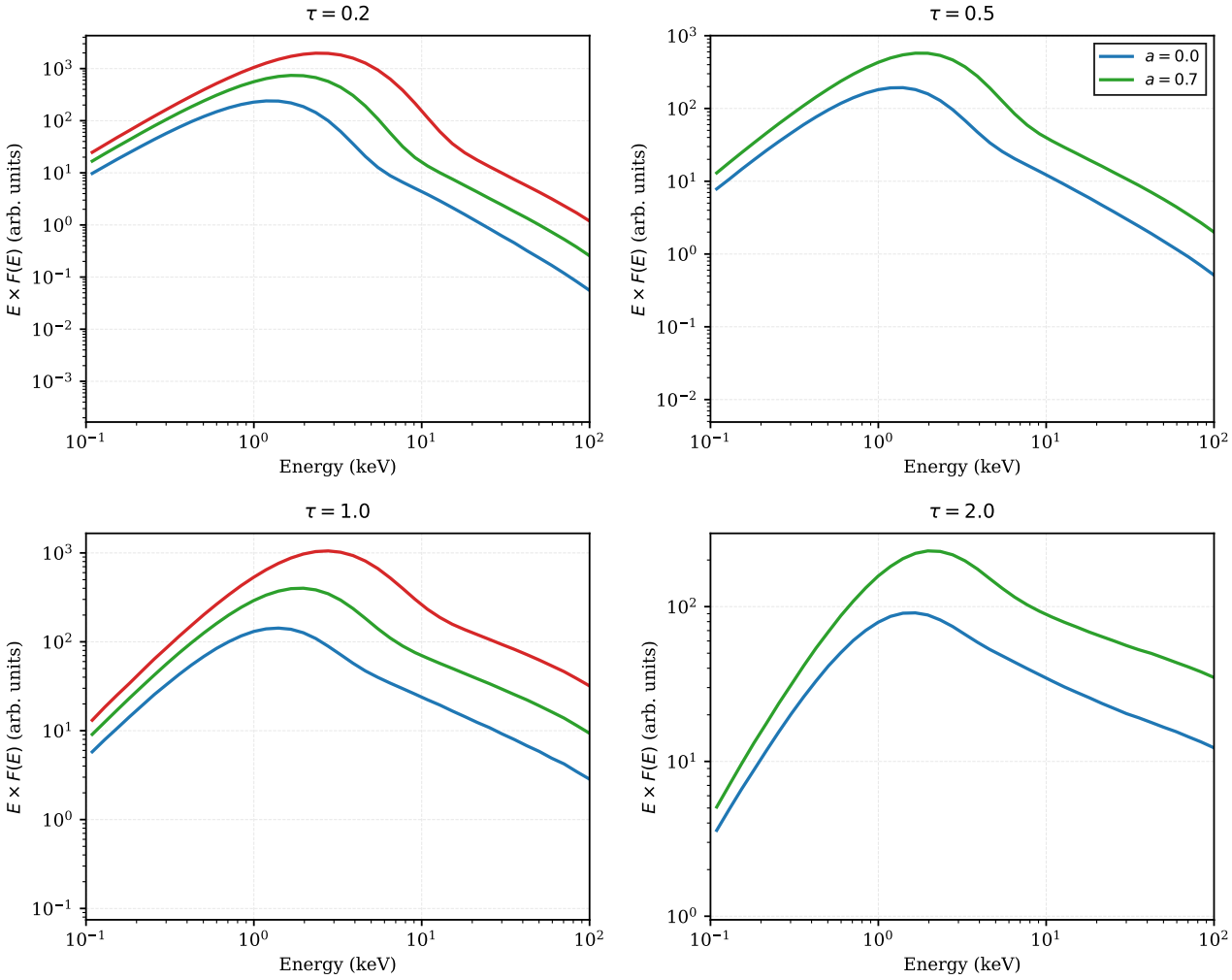


FIG. 4: Comparison of spectral shapes at fixed optical depth but varying spin. Each panel corresponds to one optical depth value ($\tau = 0.2, 0.5, 1.0, 2.0$) and shows spectra for three spins ($a = 0.0, 0.7, 0.998$). General relativistic effects are most pronounced at low optical depths, where the near-extremal case shows significant hardening ($\Delta\Gamma \approx 1.0$ at $\tau = 0.2$) due to enhanced inner-disc photon capture via gravitational light bending. At high optical depths ($\tau = 2.0$), the spectra converge as multiple scattering erases the memory of seed photon properties.

which predicts $\Gamma \approx 2.5$–3.0 at low y ($\tau \approx 0.2$–0.5) and $\Gamma \approx 1.5$–1.7 at $y \approx 1$–2 ($\tau \approx 1$–2). Our simulations broadly agree with these predictions, with measured values of Γ ranging from 3.6–3.7 at $\tau = 0.2$ to 1.6–1.7 at $\tau = 2.0$.

The slightly higher Γ values at low τ compared to classical theory can be attributed to the contribution of unscattered thermal photons in the total spectrum. When we analyze only the Comptonized component, the photon indices drop to $\Gamma_{\rm comp} \approx 2.0$–$2.2$ at $\tau = 0.2$, in better agreement with analytical predictions. This highlights the importance of properly accounting for the thermal component when comparing simulations to semi-analytical models that focus solely on scattered photons.

The optical-depth dependence found from our simulations, $\Gamma \propto \tau^{-0.45}$ [Eq. (28)], is consistent with the $\tau^{-0.5}$ scaling expected from Comptonization theory in the unsaturated regime. This agreement validates our simulation approach and confirms that the basic Comptonization physics is correctly captured despite the additional complexity of GR ray-tracing.

B. General Relativistic Effects

Our results demonstrate significant GR effects on spectral formation, particularly at low optical depths. The most striking feature is the hardening of the spectrum at $a = 0.998$ and $\tau = 0.2$, where we measure $\Gamma = 2.60 \pm 0.21$ compared to $\Gamma = 3.59 \pm 0.11$ for the Schwarzschild case. This difference of $\Delta\Gamma \approx 1.0$ is highly significant and cannot be explained by classical Comptonization theory alone.

Copyright © 2025

The physical origin of this spin-dependent hardening lies in the enhanced capture of inner-disc photons by the compact corona. At $a = 0.998$, the ISCO is located at only $1.2\,GM/c^2$ [Eq. (21)], well inside the corona's outer radius of $6\,GM/c^2$. From the disc temperature profile [Eq. (12)], the innermost disc regions at $r \approx r_{\rm ISCO}$ have:

$$T_{\rm col}(r_{\rm ISCO}) \approx 1.7 \left[\frac{3GM\dot{M}}{8\pi\sigma r_{\rm ISCO}^3} \right]^{1/4} \approx 0.8\,{\rm keV}, \tag{31}$$

for $a = 0.998$, compared to $T_{\rm col}(r_{\rm ISCO}) \approx 0.4\,{\rm keV}$ for the Schwarzschild case. These higher-energy seed photons, when Comptonized, produce a harder spectrum.

Additionally, strong gravitational light bending in the ergosphere causes a larger fraction of photons emitted from the inner disc to be directed into the corona rather than escaping directly to infinity. The photon capture efficiency can be quantified by the ratio of geodesics entering the corona to total geodesics from the disc. From our pre-computed geodesic grids, we find this ratio increases by a factor of $\sim$2 from $a = 0.0$ to $a = 0.998$ for emission from $r < 3\,GM/c^2$.

Frame-dragging effects in the Kerr metric also modify the photon trajectories and energy shifts experienced during scattering. Photons co-rotating with the black hole spin in the inner disc can gain energy through gravitational blueshift and orbital velocity effects before entering the corona, further enhancing the hardening effect.

At higher optical depths ($\tau \geq 1.0$), the spin effects become less pronounced. Multiple scatterings tend to erase the memory of the initial seed photon energy distribution, and the spectrum approaches a shape determined primarily by the electron temperature and optical depth. This convergence explains why all three spins produce similar Γ values at $\tau = 2.0$, with differences $\Delta\Gamma < 0.1$.

C. Implications for X-ray Binary Observations

Our results have several implications for interpreting XRB spectra. First, the strong optical depth dependence of the photon index provides a diagnostic for constraining coronal properties. Observed values of $\Gamma \approx 1.5$–2.0 in the hard state are consistent with moderately thick coronae with $\tau \approx 1$–2, while softer spectra with $\Gamma \approx 2.5$–3.0 suggest optically thin coronae with $\tau \approx 0.2$–0.5 or significant thermal disc contribution.

Second, the spin-dependent spectral hardening at low optical depths suggests that accurate spin measurements from continuum fitting may require proper treatment of GR effects in the corona. Existing spectral models that treat the corona with non-relativistic Comptonization may systematically bias spin estimates if the corona is compact and optically thin. Our finding that $\Delta\Gamma \approx 1.0$ between $a = 0.0$ and $a = 0.998$ at $\tau = 0.2$ implies that neglecting GR could lead to misinterpretation of spectral states. This is particularly relevant given recent high-precision spin measurements from continuum fitting [23–25] that rely on accurately modeling the inner disc emission, which can be affected by coronal properties.

Third, the energy-dependent Comptonization fraction [Eq. (27)] provides a tool for separating disc and coronal contributions in observed spectra. Spectral fitting that allows independent normalization of thermal and Comptonized components should find $f_{\rm comp}$ increasing from $\sim$0.2–0.3 at 1 keV to $\sim$0.9–1.0 above 20 keV for typical hard-state parameters ($\tau \approx 1$). This pattern can be tested with broad-band X-ray observations covering both the soft and hard bands.

Fourth, our compact corona geometry ($R = 6\,GM/c^2$) naturally produces significant spectral curvature and high-energy rollovers around 50–100 keV due to the finite electron temperature $T_{\rm e} = 100\,{\rm keV}$. The rollover energy is expected around:

$$E_{\rm cutoff} \approx 3kT_{\rm e} \approx 300\,{\rm keV}, \tag{32}$$

consistent with observed cutoff energies in XRBs [26], supporting the compact corona scenario over more extended lamppost geometries.

D. Limitations and Future Work

Our study has several limitations that should be addressed in future work. First, we have explored only one coronal geometry (spherical ZAMO corona with $R = 6\,GM/c^2$). Alternative geometries such as slab, wedge, or conical coronae may produce different spectral shapes and optical depth dependencies. Comparison with these geometries will help constrain the coronal structure in real systems.

Second, we have fixed the electron temperature at $T_{\rm e} = 100\,{\rm keV}$. Exploring a range of temperatures is essential for understanding the $T_{\rm e}$–τ degeneracy in spectral fitting and for comparison with observations showing temperature variations across different spectral states. The Comptonization parameter y [Eq. (29)] depends on both quantities, and varying them independently would map the full parameter space.

Third, our simulations do not include disc reflection, which can contribute significantly to the 5–10 keV band through iron K-shell fluorescence and Compton reflection features. Future work should incorporate reflection to produce fully self-consistent

Copyright © 2025

spectra including both direct and reflected components. The reflection fraction is expected to depend on both the coronal geometry and the black hole spin.

Fourth, our photon statistics, while adequate for spectral shape measurements, limit detailed polarization studies. Higher photon counts would enable robust polarimetric predictions for comparison with IXPE observations [8] and future X-ray polarimetry missions. The expected polarization degree from Comptonization is:

$$\Pi \approx \frac{3}{16}\frac{\tau}{1+\tau}\sin^2 i, \tag{33}$$

where i is the inclination angle, suggesting detectable levels for $\tau \sim 0.5$–1 at intermediate inclinations.

Finally, we have not yet completed the highest optical depth simulations for the near-extremal spin case ($a = 0.998$ at $\tau = 0.5$ and 2.0). These runs will allow us to fully characterize the spin–optical depth parameter space and test whether the convergence of spectral shapes at high τ holds across all spins.

E. Broader Context

This work contributes to the growing body of GR Monte Carlo simulations of black hole accretion systems [11–15]. Previous studies have explored lamppost geometries, AGN-scale systems, and polarization signatures. Our focus on compact spherical coronae in XRBs with systematic optical depth variation fills a gap in the parameter space and provides direct predictions testable with current X-ray missions such as NICER, NuSTAR, and IXPE. The compact corona geometry adopted in this study is motivated by recent X-ray reverberation observations showing corona contraction to within a few gravitational radii [4, 27] and spectral fitting studies constraining the accretion geometry in hard states [5].

The methodology employed here can be extended to explore other aspects of disc-corona physics, including time-dependent simulations of spectral state transitions, multi-temperature coronae with inhomogeneous structure, and coupled disc-corona systems where energy balance between the two components is enforced self-consistently through equations of radiative transfer and energy conservation. Such studies will move beyond the parametric approach adopted here toward more physically motivated models.

V. CONCLUSIONS

We have presented a systematic study of optical depth effects on X-ray spectral formation in compact spherical coronae surrounding stellar-mass black holes using general relativistic Monte Carlo simulations. Our main findings are:

1. The photon index decreases systematically with increasing optical depth, from $\Gamma \approx 3.6$–3.7 at $\tau = 0.2$ to $\Gamma \approx 1.6$–1.7 at $\tau = 2.0$ for the total spectrum. This trend is consistent with classical Comptonization theory predictions [Eq. (30)], with $\Delta\Gamma \approx 2.0$ over one decade in optical depth and an approximate scaling $\Gamma \propto \tau^{-0.45}$ [Eq. (28)].

2. The Comptonized component shows systematically harder spectra (lower Γ) than the total spectrum at low optical depths, where thermal emission contributes significantly. At high optical depths ($\tau \geq 1.0$), the total and Comptonized photon indices converge ($\Gamma \approx \Gamma_{\rm comp}$) as scattering dominates over direct thermal emission.

3. General relativistic effects produce significant spin-dependent spectral hardening at low optical depths. The near-extremal case ($a = 0.998$) shows $\Gamma = 2.60 \pm 0.21$ at $\tau = 0.2$, compared to $\Gamma = 3.59 \pm 0.11$ for the Schwarzschild case, a difference of $\Delta\Gamma \approx 1.0$. This hardening arises from enhanced photon capture from the hot inner disc via gravitational light bending and the smaller ISCO radius [Eq. (21)] providing higher-energy seed photons.

4. At high optical depths ($\tau = 2.0$), spin effects diminish and all cases converge toward similar spectral shapes with $\Gamma \approx 1.6$–1.7, as multiple scatterings erase the memory of seed photon properties.

5. The energy-dependent Comptonization fraction [Eq. (27)] transitions from thermal-dominated emission ($f_{\rm comp} \approx 0.1$–0.3) at soft energies ($<$1 keV) to Comptonization-dominated emission ($f_{\rm comp} \approx 0.9$–1.0) at hard energies ($>$20 keV). This energy dependence provides a diagnostic for separating disc and coronal contributions in observed spectra.

These results provide theoretical predictions for interpreting X-ray binary spectra and demonstrate the importance of including general relativistic effects when modeling compact coronae in strong-field regions. Future work will extend these simulations to additional geometries (slab, wedge, conical), temperature ranges, and include disc reflection to produce fully self-consistent spectral models for comparison with observations from current and future X-ray missions.

 Copyright © 2025

ACKNOWLEDGMENTS

We thank collaborators for helpful discussions. This research made use of computational resources at the Ulugh Beg Astronomical Institute of the Uzbek Academy of Sciences.

DATA AVAILABILITY

The simulation data and analysis scripts used in this work will be made available upon request to the corresponding author. The MONK code is available at repository URL.

REFERENCES

[1] R. A. Sunyaev and L. G. Titarchuk, A&A **86**, 121 (1980).
[2] C. Done, M. Gierliński, and A. Kubota, A&A Rev. **15**, 1 (2007).
[3] R. A. Remillard and J. E. McClintock, ARA&A **44**, 49 (2006).
[4] E. Kara, J. F. Steiner, A. C. Fabian, E. M. Cackett, P. Uttley, R. A. Remillard, K. C. Gendreau, Z. Arzoumanian, D. Altamirano, S. Eikenberry, T. Enoto, J. Homan, J. Neilsen, and A. L. Stevens, Nature **565**, 198 (2019).
[5] Y. Xu, F. A. Harrison, J. A. Tomsick, J. Hare, A. C. Fabian, D. J. Walton, K. Pottschmidt, J. A. Garcia, M. Bachetti, D. Barret, S. E. Boggs, F. E. Christensen, W. W. Craig, T. Dauser, F. Fuerst, V. Grinberg, C. J. Hailey, E. Kara, K. K. Madsen, J. M. Miller, M. L. Parker, D. Stern, J. Wilms, and W. W. Zhang, ApJ **910**, L1 (2021).
[6] A. A. Żdziarski, W. N. Johnson, and P. Magdziarz, MNRAS **283**, 193 (1996).
[7] L. Titarchuk, Astrophys. J. **434**, 570 (1994).
[8] H. Krawczynski, F. Muleri, M. Dovečiak, A. Veledina, N. Rodriguez Cavero, J. Svoboda, A. Ingram, G. Matt, J. A. Garcia, V. Loktev, M. Parra, J. F. Steiner, A. Tennant, M. Ewing, P. Kaaret, S. Kale, G. Mastroserio, J. Podgorny, F. Rao, A. Ratheesh, D. Steeghs, A. Veledina, M. C. Weisskopf, A. A. Zdziarski, and S. Zane, Science **378**, 650 (2022).
[9] A. Ingram, M. Ewing, A. Marinucci, D. Tagliacozzo, D. J. Rosario, A. Veledina, D. E. Kim, F. Marin, A. Kushwaha, W. P. Maksym, J. Piotrowska, M. Middleton, T. Dauser, J. A. Garcia, E. Kara, G. Matt, W. Alston, B. Beheshtipour, A. De Rosa, M. Dovčiak, V. E. Gianolli, H. Krawczynski, K. Madsen, G. Mastroserio, J. Podgorný, J. Steiner, F. Tombesi, F. Ursini, D. J. Walton, D. R. Wilkins, and W. Zhang, MNRAS **525**, 5437 (2023).
[10] A. Marinucci, F. Ursini, G. Matt, S. Bianchi, J. Piotrowska, M. Dovčiak, R. Middei, F. Marin, P. O. Petrucci, G. Zaino, A. Trapananti, F. Tombesi, J. Reeves, V. Braito, P. Soffitta, D. Tagliacozzo, A. Ingram, H. Krawczynski, A. Veledina, D. E. Kim, B. Beheshtipour, A. De Rosa, J. Poutanen, K. Madsen, D. J. Walton, L. Baldini, A. Di Marco, M. C. Weisskopf, A. Ratheesh, P. Kaaret, E. Costa, L. Latronico, S. R. Ehlert, J. A. García, V. E. Gianolli, F. Massaro, F. Muleri, M. Negro, J. Podgorný, K. Wu, I. Agudo, L. A. Antonelli, M. Bachetti, W. H. Baumgartner, R. Bellazzini, S. D. Bongiorno, R. Bonino, A. Brez, N. Bucciantini, F. Capitanio, S. Castellano, E. Cavazzuti, C. T. Chen, S. Ciprini, S. Citraro, L. Costamante, E. Del Monte, L. Di Gesu, N. Di Lalla, I. Donnarumma, V. Doroshenko, T. Enoto, Y. Evangelista, S. Fabiani, R. Ferrazzoli, S. Gunji, K. Hayashida, J. Heyl, W. Iwakiri, S. G. Jorstad, V. Karas, T. Kitaguchi, J. J. Kolodziejczak, F. La Monaca, I. Liodakis, S. Maldera, A. Manfreda, A. P. Marscher, H. L. Marshall, I. Mitsuishi, T. Mizuno, C. Y. Ng, S. L. O'Dell, N. Omodei, C. Oppedisano, A. Papitto, G. G. Pavlov, A. L. Peirson, M. Perri, M. Pesce-Rollins, M. Pilia, A. Possenti, S. Puccetti, B. D. Ramsey, J. Rankin, O. J. Roberts, R. W. Romani, C. Sgrò, P. Slane, G. Spandre, D. A. Swartz, T. Tamagawa, F. Tavecchio, R. Taverna, Y. Tawara, A. F. Tennant, N. E. Thomas, A. Trois, S. S. Tsygankov, R. Turolla, J. Vink, F. Xie, and S. Zane, A&A **688**, A155 (2024).
[11] W. Zhang, M. Dovčiak, and M. Bursa, MNRAS **488**, 5412 (2019).
[12] G. Mastroserio, A. Ingram, F. Jimenez-Ibarra, J. van den Eijnden, K. Alabarta, K. Koljonen, T. D. Russell, M. C. Baglio, D. M. Bramich, S. Campana, P. Casella, C. Ceccobello, S. Covino, T. Dincer, R. Fender, P. G. Jonker, F. Lewis, T. J. Maccarone, M. Méndez, T. Muñoz-Darias, J. A. Paice, A. F. Pala, S. A. Pirbhoy, P. Saikia, A. Sanna, T. Shahbaz, M. A. P. Torres, and F. Vincentelli, arXiv e-prints , arXiv:2508.21511 (2024), arXiv:2508.21511.
[13] J. D. Schnittman and J. H. Krolik, Astrophys. J. **712**, 908 (2010).
[14] J. D. Schnittman and J. H. Krolik, Astrophys. J. **769**, 156 (2013).
[15] M. Dovčiak, F. Muleri, R. W. Goosmann, V. Karas, and G. Matt, MNRAS **416**, 2095 (2011).
[16] J. Podgorný, M. Dovčiak, F. Marin, R. W. Goosmann, A. Różańska, G. Matt, E. S. Kammoun, S. Bianchi, A. Marinucci, F. Ursini, R. Middei, F. Tamborra, and S. Bhutani, MNRAS **510**, 4723 (2022).
[17] I. D. Novikov and K. S. Thorne, Black Holes (Les Astres Occlus) , 343 (1973).
[18] D. N. Page and K. S. Thorne, Astrophys. J. **191**, 499 (1974).
[19] M. Walker and R. Penrose, Communications in Mathematical Physics **18**, 265 (1970).
[20] P. A. Connors, R. F. Stark, and T. Piran, Astrophys. J. **235**, 224 (1980).
[21] A. Veledina, J. Poutanen, and I. Vurm, Astrophys. J. **884**, 144 (2019).

Copyright © 2025

[22] J. Poutanen, A. Veledina, and A. A. Zdziarski, MNRAS **536**, 603 (2024).
[23] X. Zhao, L. Gou, Y. Dong, X. Zheng, J. F. Steiner, J. E. McClintock, R. Narayan, N. Jia, and Z. Yu, Astrophys. J. **908**, 117 (2021).
[24] J. E. McClintock, R. Narayan, and J. F. Steiner, Space Sci. Rev. **183**, 295 (2014).
[25] J. F. Steiner, J. E. McClintock, R. A. Remillard, R. Narayan, and L. Gou, ApJ **701**, L83 (2009).
[26] E. Jourdain, J. P. Roques, M. Chauvin, and D. J. Clark, Astrophys. J. **789**, 26 (2014).
[27] E. Nathan, A. Ingram, E. Kara, R. M. T. Connors, T. Dauser, J. A. García, J. A. Tomsick, M. Lucchini, J. Wang, G. Mastroserio, R. Connors, P. Uttley, D. J. K. Buisson, D. Barret, A. C. Fabian, F. A. Harrison, R. A. Remillard, D. J. Walton, and J. Wilms, MNRAS **511**, 255 (2022).

 Copyright © 2025